



Multi-component nanoporous platinum–ruthenium–copper–osmium–iridium alloy with enhanced electrocatalytic activity towards methanol oxidation and oxygen reduction

Xiaoting Chen^a, Conghui Si^a, Yulai Gao^b, Jan Frenzel^c, Junzhe Sun^a, Gunther Eggeler^c, Zhonghua Zhang^{a, b, *}

^a Key Laboratory for Liquid–Solid Structural Evolution and Processing of Materials (Ministry of Education), School of Materials Science and Engineering, Shandong University, Jingshi Road 17923, Jinan 250061, PR China

^b Shanghai Key Laboratory of Modern Metallurgy and Materials Processing, Shanghai University, 200072 Shanghai, PR China

^c Institut für Werkstoffe, Ruhr Universität Bochum, Bochum 44780, Germany

HIGHLIGHTS

- Np-PtRuCuOsIr alloy can be fabricated by ball-milling and subsequent dealloying.
- Np-PtRuCuOsIr shows superior activity and CO tolerance towards methanol oxidation.
- Np-PtRuCuOsIr shows greatly enhanced catalytic activity and durability toward ORR.

ARTICLE INFO

Article history:

Received 22 June 2014

Received in revised form

27 August 2014

Accepted 10 September 2014

Available online 18 September 2014

Keywords:

Direct methanol fuel cells

Electro-oxidation

Oxygen reduction reaction

Dealloying

Nanoporous alloys

ABSTRACT

Multi-component nanoporous platinum–ruthenium–copper–osmium–iridium (np-PtRuCuOsIr) electrocatalyst has been facilely fabricated by chemical dealloying of mechanically alloyed AlCuPtRuOsIr precursor. The np-PtRuCuOsIr catalyst exhibits a typical three-dimensional bi-continuous interpenetrating ligament/channel structure with a length scale of ~2.5 nm. The np-PtRuCuOsIr catalyst reaches a higher level in the mass activity (857.5 mA mg_{Pt}^{−1}) and specific activity (3.0 mA cm^{−2}) towards methanol oxidation compared to the commercial PtC catalyst (229.5 mA mg_{Pt}^{−1} and 0.5 mA cm^{−2} respectively). Moreover, the CO stripping peak of np-PtRuCuOsIr is 0.54 V (vs. SCE), 130 mV negative shift in comparison with the commercial PtC (0.67 V vs. SCE). The half-wave potential of np-PtRuCuOsIr is 0.900 V vs. RHE, 36 mV positive compared with that of the commercial PtC (0.864 V vs. RHE). The np-PtRuCuOsIr catalyst also shows 1.8 and 3.8 times enhancement in the mass and specific activity towards oxygen reduction than the commercial PtC. Moreover, the np-PtRuCuOsIr alloy exhibits superior oxygen reduction activities even after 15 K cycles, indicating its excellent long-term stability. The present np-PtRuCuOsIr can act as a promising candidate for the electrocatalyst in direct methanol fuel cells (DMFCs).

© 2014 Elsevier B.V. All rights reserved.

1. Introduction

Direct methanol fuel cells (DMFCs) are promising future energy devices alternative to conventional energy generating

* Corresponding author. Key Laboratory for Liquid–Solid Structural Evolution and Processing of Materials (Ministry of Education), School of Materials Science and Engineering, Shandong University, Jingshi Road 17923, Jinan 250061, PR China. Tel./fax: +86 531 88396978.

E-mail address: zh_zhang@sdu.edu.cn (Z. Zhang).

counterparts, because of their low pollutant emission, availability of methanol fuel, easy distribution and high energy-conversion efficiency of the fuel [1–5]. As an important component, the state-of-the-art electrocatalysts must ensure the methanol oxidation reaction (MOR) at anode and oxygen reduction reaction (ORR) at cathode to generate electricity with water and carbon dioxide as the by-products [5,6]. As of now, Pt catalysts are still the well-known and commonly-adopted materials for DMFCs. However, major shortcomings hindering the successful application of DMFCs are low activity, serious CO poisoning, sluggish ORR kinetics and

poor durability of Pt-based catalysts. To decrease the addition amount of Pt and enhance its utilization efficiency, one common strategy is to synthesize Pt-containing nanocatalysts through alloying Pt with other nonprecious metals. Over the past decade, incorporating other metals (e.g. Ru [7–9], Ni [10,11], Co [11,12], Fe [13], Cu [14] and Pd [15,16]) with platinum to generate alloyed nanostructures represents a robust approach toward improved catalytic performance. Among these, PtRu catalysts were believed to be the more suitable catalysts due to their completely rapid, two-step oxidation mechanism [17,18]. Moreover, it has been found that the compositional improvement of alloying elements substantially boosts the catalytic properties of electrocatalysts. Until recently, sufficient efforts have been devoted to the synthesis of PtRu-based catalysts [3,6,19–21] compared to other Pt catalysts. For example, Reddington et al. [6] brought a breakthrough in finding that multicomponent PtRuOsIr alloy catalyst exhibits significantly higher activity than PtRu. Whitacre et al. [22] also investigated a low Pt loaded catalyst ($\text{Ni}_{31}\text{Zr}_{13}\text{Pt}_{33}\text{Ru}_{23}$) with great activity towards MOR.

On the other side, the commercialization of DMFCs awaits not only efficient usage of platinum, but cost-effective preparation methods and techniques. Various synthetic strategies, such as microemulsions [9,21], microwave irradiation [23–25], electrodeposition [26] and chemical reduction [6,27] have been employed to prepare alloy electrocatalysts including multiple elements. However, all of these include meticulous chemical steps, use costly surfactant molecules, and require a substantial number of separation and washing steps [21,28]. This turns down the hope to have as many 3d metals as possible in the alloy catalyst for performance improvement and reduction of cost. Consequently these methods lead to the rather high threshold of large-scale production and application. Dealloying, during which an alloy is ‘parted’ by the selective dissolution of the most electrochemically active element(s) and the retaining noble one evolves to a bi-continuous structure of metal-and-void with an average ligament size at the nanoscale level [29]. This technique has recently been receiving considerable attention for tailoring nanoporous metallic materials with high specific surface areas aiming at acquiring improved properties in various fields such as sensing [30], actuation [31] and catalytic properties towards small organic molecules [32,33]. To date, nanoporous metals (e.g. Cu [34], Pd [35,36], Ag [37,38] etc.) and alloys (e.g. PdNi [32,33], PdCo [36], PtCu [39], PtAu [28,40] etc.) have been successfully synthesized through dealloying. In addition, morphological aspects and underlying physical mechanisms of dealloying process have also aroused considerable attention [29]. Our group has successfully fabricated a series of alloy nanostructures through this rapid and simple method [28,32,38,41].

In the present investigation, the peculiar nanoporous structures of np-PtRuCuOsIr can be directly fabricated by mild chemical dealloying of multicomponent AlCu-based precursor alloy which was obtained through a simple mechanical alloying process. The facile and green technique shows great advantages in the design of nanostructured alloy electrocatalysts: (i) the combination of mechanical alloying with dealloying could reduce the complexity and limitation to design various multiple-component nanoporous alloys, (ii) the nanoporous alloy catalysts can be produced in mass (dozens of grams) to meet the requirement of commercialization of electrocatalysts, (iii) the obtained unique three-dimensional bi-continuous interpenetrating ligament/channel structure proves to be ideal to the electro-catalytic reaction including MOR and ORR. This new catalyst was characterized with electrochemical measurements at the anode as well as the cathode for DMFCs. Our testing results show that the np-PtRuCuOsIr catalyst performs far better than the commercial PtC catalyst. Considering the advantages of design technology as well as the enhanced electrocatalytic

activities, this novel np-PtRuCuOsIr alloy is expected to act as a promising electrocatalyst in the DMFCs.

2. Experimental section

To achieve easy dealloying and good control for the resulting alloy composition, a multi-component $\text{Al}_{66}\text{Cu}_{30}(\text{Pt}_{44}\text{Ru}_{41}\text{Os}_{10}\text{Ir}_5)_4$ alloy (nominal composition, at.%) was chosen as the precursor. The starting $\text{Al}_{66}\text{Cu}_{30}(\text{Pt}_{44}\text{Ru}_{41}\text{Os}_{10}\text{Ir}_5)_4$ alloy powders was prepared from pure Al, Cu, Pt, Ru, Os and Ir (99.9 wt.%) powders using a planetary ball milling machine. Then dealloying of the $\text{Al}_{66}\text{Cu}_{30}(\text{Pt}_{44}\text{Ru}_{41}\text{Os}_{10}\text{Ir}_5)_4$ alloy powders was performed in a 1 M HNO_3 solution at room temperature until no obvious bubbles emerged. After the facile dealloying, the as-dealloyed samples were rinsed in distilled water and dehydrated alcohol to gain the final np-PtRuCuOsIr.

X-ray diffractograms of the mechanically alloyed $\text{Al}_{66}\text{Cu}_{30}(\text{Pt}_{44}\text{Ru}_{41}\text{Os}_{10}\text{Ir}_5)_4$ precursor and as-dealloyed samples were obtained by an X-ray diffractometer (XRD, Rigaku D/max-rB) with Cu K α radiation. The chemical compositions of the as-dealloyed samples were determined by an energy-dispersive X-ray (EDX) analyzer in an area-analysis mode (a typical area of $50\text{ }\mu\text{m} \times 50\text{ }\mu\text{m}$), in order to accurately obtain the compositions of the samples. At least three areas were analyzed and the average values were given in the results. The microstructure of the as-dealloyed catalyst was characterized using a transmission electron microscope (TEM, FEI Tecnai G2), and high-resolution TEM (HRTEM, FEI Tecnai G2). In addition, selected-area electron diffraction (SAED) patterns were also obtained. The fast Fourier transform (FFT) patterns were obtained from the corresponding HRTEM images using a software named Gatan Digital Micrograph.

All electrochemical measurements were carried out in a standard three-electrode cell with a CHI 760E Potentiostat. A saturated calomel electrode (SCE) was used as the reference electrode and a bright Pt plate was used as the counter electrode for the electrochemical measurements of methanol electro-oxidation. We benchmarked the electrochemical properties of the np-PtRuCuOsIr against the commercial (Johnson's Matthey) PtC (40 wt.%) catalyst under the identical experimental conditions. The catalyst ink was prepared as follows: 2.0 mg of the synthesized alloy, 3.0 mg XC-72 carbon powder, 1.5 mL isopropanol and 0.5 mL Nafion solution (0.5 wt.%) were ultrasonically mixed for 30 min. Afterward, 4 μL homogeneously mixed catalyst suspension was dropped on a freshly polished glassy carbon (GC) electrode with a diameter of 4 mm (apparent surface area, 0.126 cm^2). The loading of Pt for the commercial PtC catalyst was $31.7\text{ }\mu\text{g}_{\text{Pt}}\text{ cm}^{-2}$ and that for the np-PtRuCuOsIr was $18.0\text{ }\mu\text{g}_{\text{Pt}}\text{ cm}^{-2}$ (with total metal loading of $31.7\text{ }\mu\text{g cm}^{-2}$), which were consistent with some examined electrocatalysts in the literature [42,43]. The coated GC electrode was used as the working electrode after drying in a vacuum tank at room temperature for at least 3 h. The cyclic voltammetry (CV) behavior of the catalyst was determined in a 0.5 M H_2SO_4 solution deaerated with N_2 . Several scans were performed until reproducible voltammograms were obtained. The electrocatalytic activity of the as-prepared catalyst for the methanol oxidation was characterized in a N_2 -purged 0.5 M $\text{H}_2\text{SO}_4 + 0.5\text{ M CH}_3\text{OH}$ solution at $30\text{ }^\circ\text{C}$. The CO tolerance was characterized by CO stripping firstly maintaining the working electrode in the 0.5 M H_2SO_4 solution saturated with bubbling CO gas for the period of 500 s. After CO adsorption, the electrode was transferred into a CO-free 0.5 M H_2SO_4 solution followed by potential scanning between -0.21 and 1.06 V (vs. SCE).

In the cathode scanning, a rotating disk electrode (RDE) technique was employed to electrochemically evaluate the ORR process of the catalyst. A reversible hydrogen electrode (RHE) and a rotating

disk electrode with a diameter of 5 mm (geometric surface area, 0.196 cm^2) were used as the reference and working electrodes, respectively. The loadings of Pt for the commercial PtC catalyst and np-PtRuCuOsIr were determined to be 18.0 and $25.0 \mu\text{g}_{\text{Pt}}^{-1} \text{ cm}^{-2}$ respectively, similar with the reports in the literature [33,44]. The electrochemical properties of the catalyst in a N_2 -saturated 0.1 M HClO_4 were first studied by cyclic voltammetry to obtain a stable cyclic voltammogram in order to determine the electrochemically active surface area (ECSA) of the catalyst. Then, the ORR experiment was performed under a rotation speed of 1600 rpm at a scan rate of 10 mV s^{-1} . Saturation with high purity oxygen was performed prior to the electrocatalytic activity measurement. The durability testing was performed under half-cell conditions in the 0.1 M HClO_4 solution, utilizing the protocol described by many researchers [33,45,46]. The np-PtRuCuOsIr electrode was cycled from 0.6 to 1.0 V vs. RHE at a scan rate of 50 mV s^{-1} in the 0.1 M HClO_4 solution and left open to the atmosphere to allow for the replenishment of the dissolved oxygen in the electrolyte. The ECSA and electrochemical activities were measured after 10, 10 K and 15 K cycles.

3. Results and discussion

3.1. Microstructural characterization of np-PtRuCuOsIr

Fig. 1 shows the XRD patterns of the $\text{Al}_{66}\text{Cu}_{30}(\text{Pt}_{44}\text{Ru}_{41}\text{Os}_{10}\text{Ir}_5)_4$ precursor alloy and the as-dealloyed samples. As shown in Fig. 1a, a number of diffraction peaks appear on the pattern of the as-milled $\text{Al}_{66}\text{Cu}_{30}(\text{Pt}_{44}\text{Ru}_{41}\text{Os}_{10}\text{Ir}_5)_4$ precursor, which can be ascribed to a Al_4Cu_9 -type (PDF No. 65-3347) intermetallic phase. However, there are some diffraction peaks with relative intensity and peak position different from the diffraction profile of standard Al_4Cu_9 -type intermetallic phase, which may be caused by different alloy composition and fabrication process [33]. In addition, for multi-component alloys, some metastable and/or amorphous phases will occur during mechanical alloying. After dealloying in the HNO_3 solution, the XRD pattern illustrates four broadened Bragg peaks located at scattering angles (2θ) of ca. 39.8, 46.2, 67.6 and 81.8° (Fig. 1b). These peaks correspond to the face-centered cubic (f.c.c.) Pt (PDF No. 04-0802) in spite of the shifting of Bragg peaks. This is understandable to assume that the alloying elements (Cu, Os, Ir, Ru) exist in the Pt phase in the form of solid solution. Thus the incorporation will lead to a change in the lattice or d spacing compared to pure Pt. It's consistent with the report that incorporation of other metals would lead to a more pronounced change in the form and position of the Pt diffraction peaks [27]. In addition, some diffraction peaks have coincident angles with the hexagonal structure of (Os, Ir, Ru) solid solution (PDF No. 41-0602) and Ru (PDF No. 06-0663), Fig. 1b. We hold the opinion that a little amount of Ru failed to be alloyed and remained in the as-dealloyed samples. This conjecture will be verified by TEM observation as described in the following. Additionally, the chemical composition of the as-dealloyed samples was determined by EDX and one typical spectrum is presented in Fig. 1c. The corresponding results reveal that the as-dealloyed sample is mainly composed of Pt (45.8 at.%), Ru (19.2 at.%), Cu (16.0 at.%), Os (11.6 at.%) and Ir (7.4 at.%). And only a minor residual Al (few atom percent) could be detected in the as-dealloyed samples.

On the basis of TEM observation (Fig. 2a), the as-dealloyed samples clearly display an interconnected nanoscaled backbone (metal) and bi-continuous channels (void) in all three dimensions with a typical ligament size of around 2.5 nm. Besides the ultrafine ligament/channel structure of the as-dealloyed samples, the SAED analysis confirms the nanocrystalline nature of the as-dealloyed samples across the whole selected area (around 200 nm in diameter), inset of Fig. 2a. The corresponding SAED pattern can be

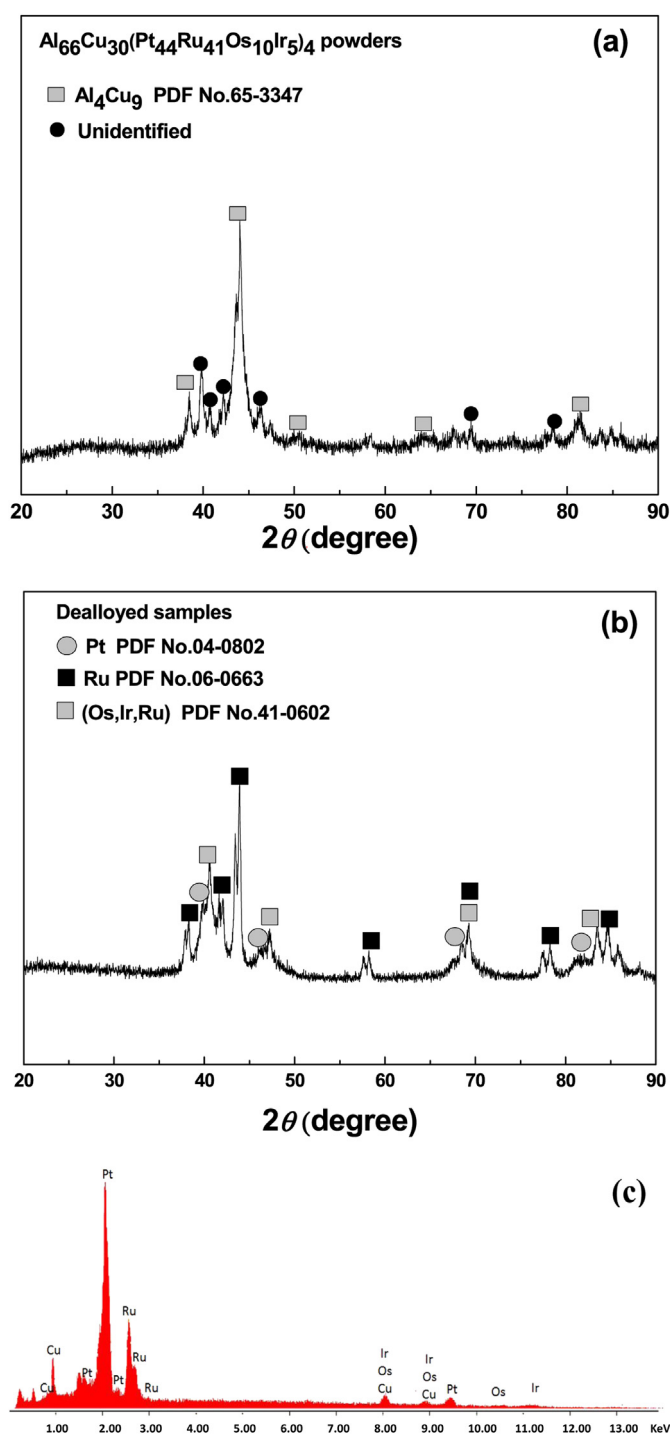


Fig. 1. XRD patterns of (a) the mechanically alloyed $\text{Al}_{66}\text{Cu}_{30}(\text{Pt}_{44}\text{Ru}_{41}\text{Os}_{10}\text{Ir}_5)_4$ powders and (b) the as-dealloyed samples obtained by dealloying the powders in the 1 M HNO_3 solution at room temperature. (c) A typical EDX spectrum of the as-dealloyed samples.

indexed as (111), (200), (220) and (311) reflections of f.c.c. Pt. In some areas, nanoparticles of 10–20 nm in size can also be observed and one particle is highlighted by a dotted circle in Fig. 2b. These nanoparticles are embedded in the nanoporous matrix. The corresponding SAED pattern (inset of Fig. 2b) consists of polycrystalline diffraction rings and single crystal diffraction spots. The diffraction rings come from the nanoporous matrix (f.c.c. Pt solid solution), and the diffraction spots originate from the embedded

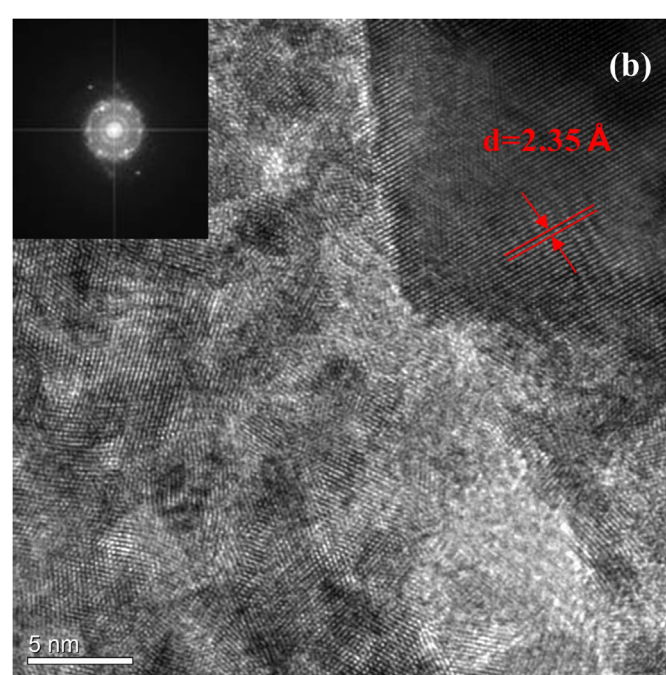
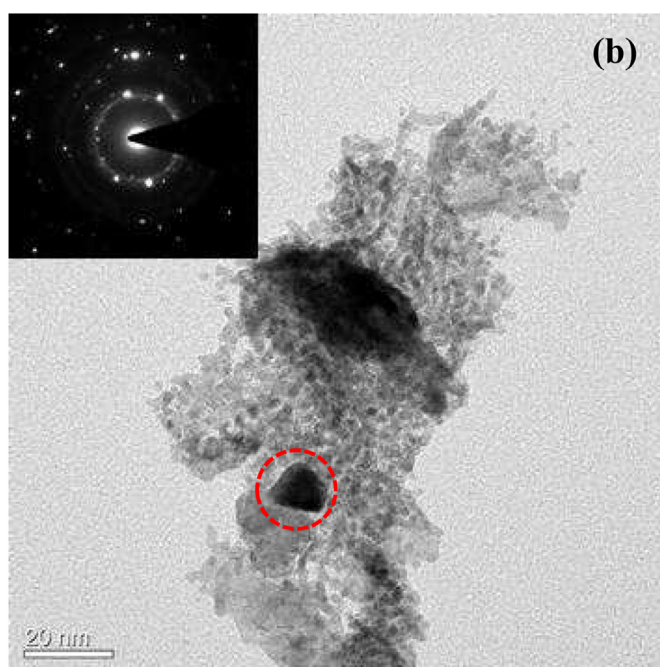
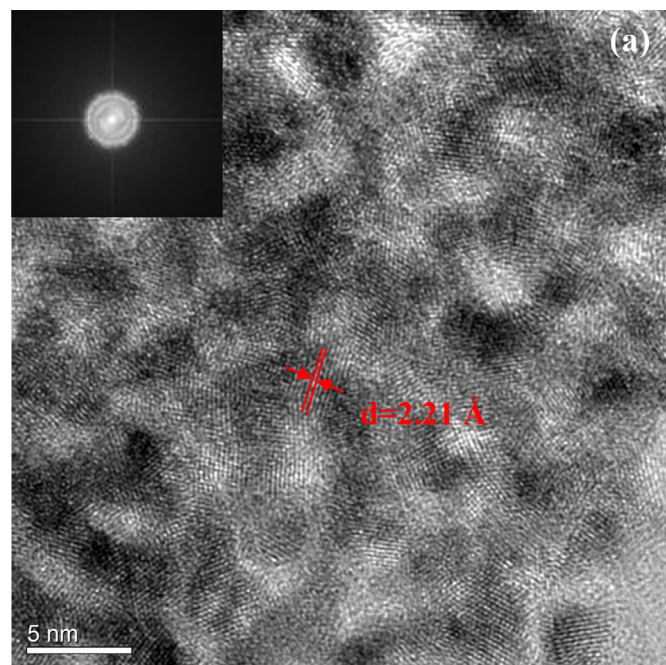
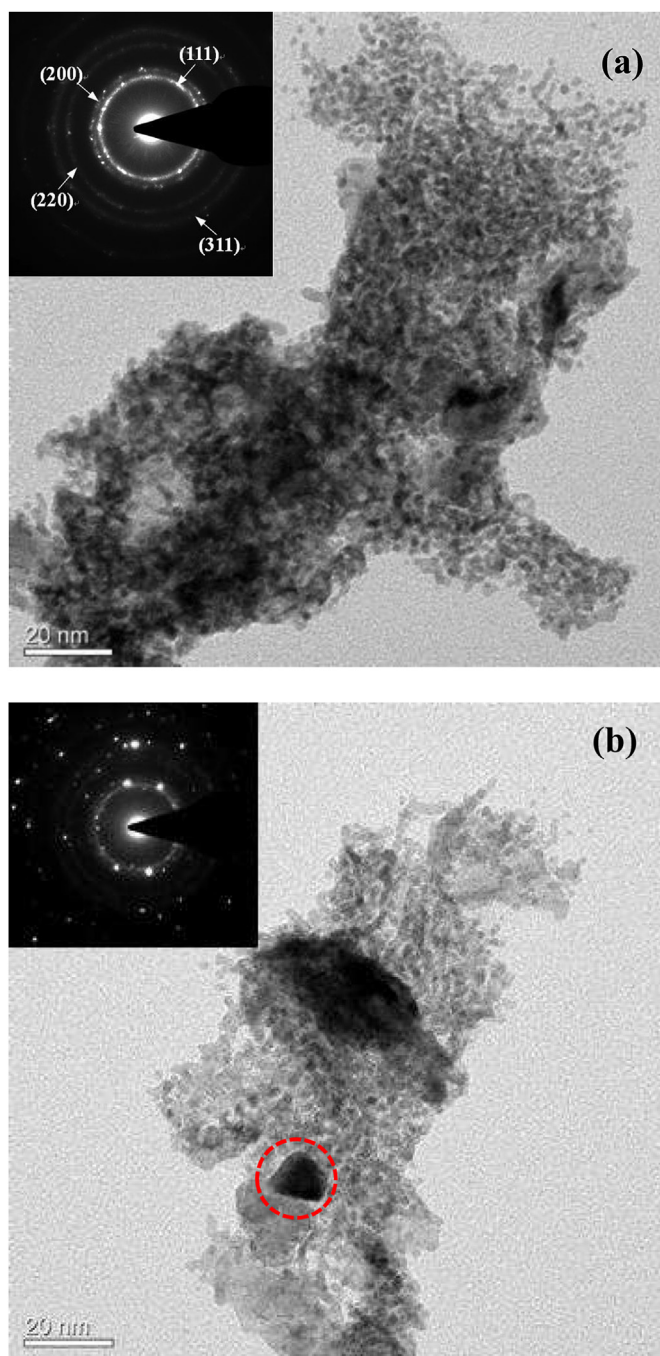


Fig. 2. (a, b) TEM images showing the nanoporous microstructure of the np-PtRuCuOsIr alloy fabricated by the dealloying method, insets in (a, b): corresponding SAED patterns.

nanoparticles, which correspond to the (002) plane of the (Os,Ir,Ru) and Ru phases. Overall, the TEM results are in agreement with the XRD results (Fig. 1b).

Fig. 3 shows the HRTEM images and corresponding FFT patterns of the as-dealloyed samples. The typical bi-continuous ligament-channel structure can be clearly observed (Fig. 3a). The ligaments are composed of small nanocrystals of several nanometers in size, and the spacing of some lattice fringes is 0.221 nm (Fig. 3a), which is close to (111) crystal plane of f.c.c. Pt (~0.226 nm). The HRTEM image and FFT pattern (inset in Fig. 3a) further verify the nanocrystalline nature of the connected ligaments. Fig. 3b shows the

Fig. 3. (a, b) HRTEM images of the np-PtRuCuOsIr alloy, insets in (a, b): corresponding FFT patterns.

HRTEM image of another area. Both the nanoporous structure and a little larger nanoparticle can be seen. Furthermore, regular lattice fringes run across the whole nanoparticle and the lattice spacing was calculated to be 0.235 nm (as indicated in Fig. 3b), which is close to the value of Ru (100) crystal plane (0.234 nm) and (Os,Ir,Ru) (100) crystal plane (0.236 nm). The corresponding FFT pattern is presented in the inset of Fig. 3b. Both the XRD and TEM/SAED results confirm that partial Ru failed to be alloyed with Pt in the np-PtRuCuOsIr samples. It has been reported that the mixing of Pt and Ru nanoparticles instead of nanoporous alloy was usually obtained [8]. In addition, the mixing enthalpy is an important parameter for the formation and stability of the intermediate phase. The enthalpy

of mixing in Pt–Ru system (ΔH_{mix}) is 6 kJ mol^{-1} [47], indicating the difficulty to form an alloy between these two elements.

It is known that the less noble (with a smaller redox potential) element experiences corrosive dissolution and the more noble one diffuses and re-organizes during the dealloying process. This will lead to the formation of a nanoporous bi-continuous structure of metal-and-void [29]. When dealloying in the HNO_3 solution, almost all the Al and partial Cu are dissolved, while minimizing the dissolution of the more noble elements. Moreover, by comparison with the composition of the precursor alloy, it has been found that partial Ru is also leached out during the dealloying process. The as-dealloyed samples can be designated as np-PtRuCuOsIr for simplicity.

3.2. Catalytic activity of np-PtRuCuOsIr towards methanol oxidation

In general, conducting a potential cycling can not only clean the catalyst surface to improve its reactivity but also reveal some important electrochemical features, such as the typical under-potentially deposited hydrogen ad/desorption, double layer and metallic redox region [48]. Normally, the electrochemically active surface area (ECSA) can be calculated by integrating the hydrogen ad/desorption charge and assuming a value of 210 C cm^{-2} for the oxidation of a monolayer of hydrogen on a polycrystalline Pt electrode [48]. Especially, for some typical multi-metallic nanoparticle catalysts, the potential cycling can even induce the leaching of less-noble metals in an acidic circumstance and contribute to some changes of the nanoparticles [15,27,46]. Hence, a similar voltammetric pretreatment (or activation) has been performed on these as-prepared np-PtRuCuOsIr and commercial PtC catalysts prior to the activity measurement. For np-PtRuCuOsIr, a dissolution peak can be observed with the potential sweeping anodically in the first scan (Fig. 4a). In the subsequent scans, the dissolution peak gradually decreases in intensity while H ad/desorption features gradually emerge to form the final stable curve as shown in Fig. 4a. During the initial CV cycles, a Pt-rich skin would form on the ligament surface accompanying the dissolution of the active elements (such as Cu and the residual Al), which in turn would prevent the active elements in the underlying layer from further dissolving [23,39,49]. Interestingly, the shape and higher oxide potential of the dissolution peak were typical to PtRu alloys, which have been studied sufficiently by Yoo et al. [50]. Thus, it is reasonable to assume the dissolution of the un-alloyed Ru from the catalyst surface during the potential cycling. Fig. 4b shows the final cyclic voltammetry (CV) curves of np-PtRuCuOsIr and PtC catalysts in the 0.5 M H_2SO_4 solution with typical profile features. As shown in Fig. 4b, the final time-stable profile of np-PtRuCuOsIr exhibits changes including (i) the broader double electric layer and featureless shoulder region from -0.20 to 0.20 V (vs. SCE), and (ii) the positive shifting of the peak position for the reduction of Pt oxides compared to the PtC catalyst in the back scan (as indicated by dotted line in Fig. 4b). As for the multi-component np-PtRuCuOsIr, it is reasonable to assume that the co-existence of alloying elements (Ru,Cu,Os,Ir) greatly affects the exposed Pt atoms on the surface. Thus, the obtained CV profile of np-PtRuCuOsIr is different from that of the commercial PtC catalyst (Fig. 4b). The CV features of np-PtRuCuOsIr are in good agreement with the literature [15,20,27,46], in which Pt-based alloys have been successfully fabricated. According to the calculation method, the ECSAs of the np-PtRuCuOsIr alloy and PtC catalyst were determined to be 29 and $47 \text{ m}^2 \text{ g}^{-1}$, respectively.

The np-PtRuCuOsIr catalyst exhibits significantly enhanced electrocatalytic activity towards the methanol oxidation. Fig. 5a and b shows the ECSA- and Pt mass-normalized CVs for the np-

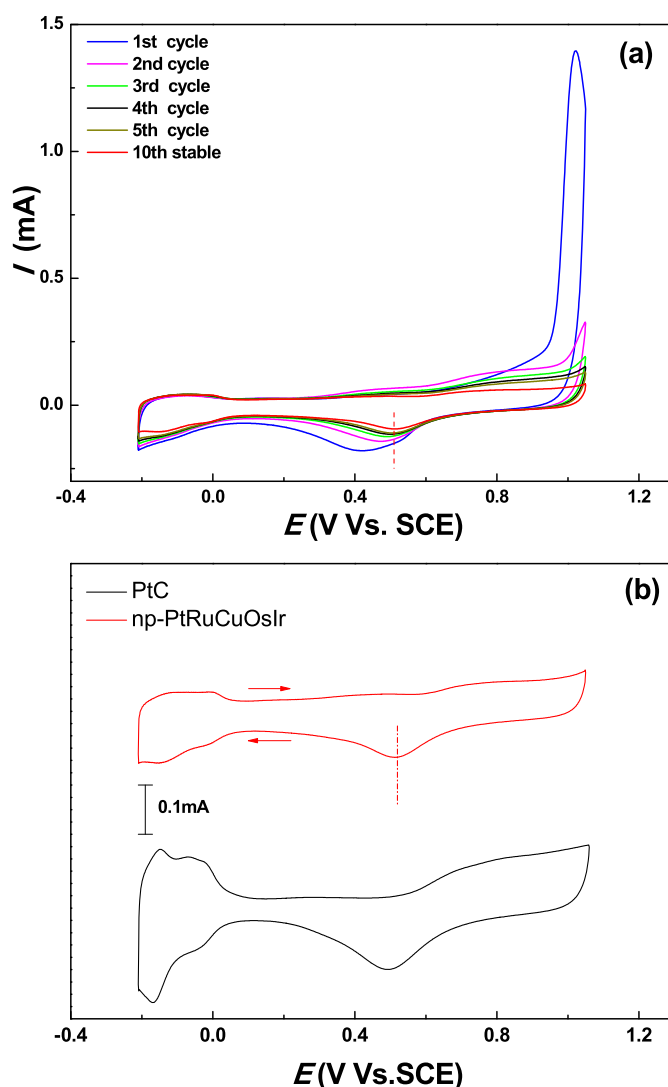


Fig. 4. (a) The evolution of initial cyclic voltammetric curves of the np-PtRuCuOsIr alloy and (b) stable CVs of the np-PtRuCuOsIr and PtC catalysts in the N_2 purged 0.5 M H_2SO_4 solution (scan rate: 50 mV s^{-1}).

PtRuCuOsIr alloy and PtC catalyst in the 0.5 M $\text{H}_2\text{SO}_4 + 0.5 \text{ M}$ CH_3OH solution, respectively. It can be seen that the peak potential is 0.61 V (vs. SCE) for the np-PtRuCuOsIr in the forward scan, which is slightly lower than that (0.62 V vs. SCE) of PtC. Moreover, the onset potentials are comparable for both catalysts. The current densities in the forward scan are normally utilized to assess the electrocatalytic activity of catalysts. As shown in Fig. 5a, the specific activity (in the forward scan) of the np-PtRuCuOsIr is 3.0 mA cm^{-2} , which is 6 times that of the PtC catalyst (0.5 mA cm^{-2}). For easy to further comparison, we used similar catalyst loading, and the plot was normalized with the Pt mass. The activity of the state-of-the-art of low Pt loading electrocatalysts for MOR is between $250 \text{ mA mg}_{\text{Pt}}^{-1}$ and $1000 \text{ mA mg}_{\text{Pt}}^{-1}$, and a large number of catalysts exhibit even lower activities ($<250 \text{ mA mg}_{\text{Pt}}^{-1}$) [43]. As shown in Fig. 5b, the np-PtRuCuOsIr catalyst shows the higher MOR activity of $857.5 \text{ mA mg}_{\text{Pt}}^{-1}$, which is about 3.7 times of that for PtC ($229.5 \text{ mA mg}_{\text{Pt}}^{-1}$). The activity of the as-obtained catalyst is also comparable to the data reported elsewhere [51]. Generally speaking, the electro-oxidation of methanol molecules leads to the formation of current peak near 0.6 V (vs. SCE) in the forward scan. Mancharan and Goodenough [52] have suggested that the anodic

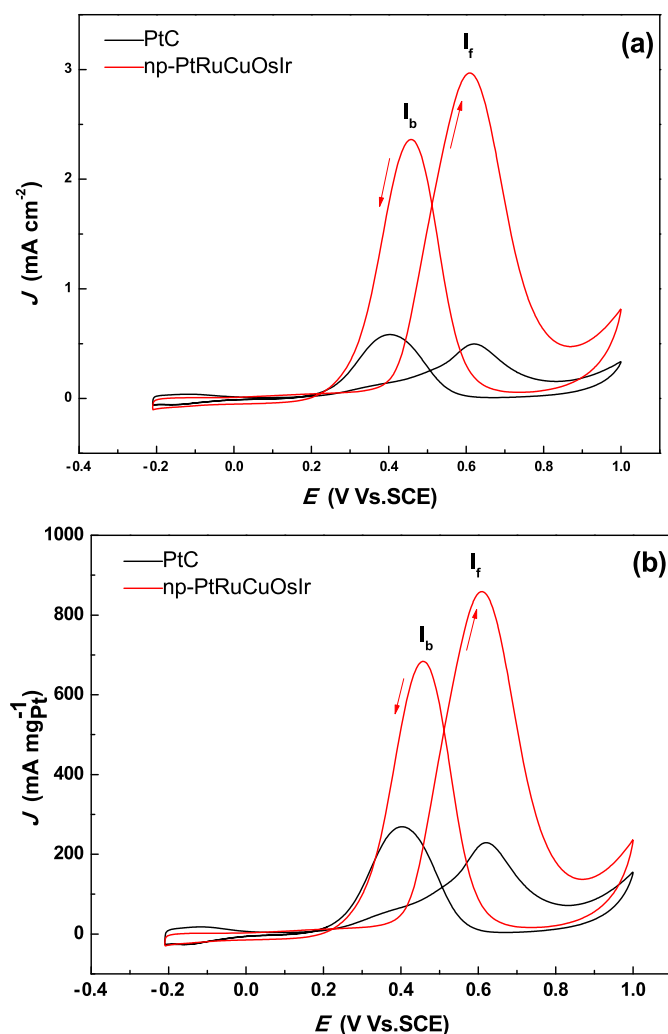


Fig. 5. (a) ECSA-normalized and (b) mass-normalized CVs of the np-PtRuCuOsIr and PtC catalysts for methanol electro-oxidation in the 0.5 M H_2SO_4 + 0.5 M CH_3OH solution at 30 °C (scan rate: 50 mV s^{-1}).

peak in the reverse scan might be attributed to the removal of the incompletely oxidized carbonaceous species such as CO. Hence, the ratio of the forward anodic peak current density (I_f) to the reverse anodic peak current density (I_b) is usually used to describe the tolerance of the catalyst to accumulation of carbonaceous species [13,15,39]. The high I_f/I_b indicates an excellent oxidation of methanol during the forward anodic scan and less accumulation of residues on the catalyst. The I_f/I_b ratio of 1.26 for the np-PtRuCuOsIr alloy is much higher than 0.91 for PtC, which indicates less accumulation of residues on the np-PtRuCuOsIr catalyst during methanol oxidation compared to the commercial PtC catalyst. However, there exist controversies over the use of I_f/I_b to evaluate the CO tolerance of Pt-based electrocatalysts. Most recently, Hofstead-Duffy et al. [53] have argued that the use of the I_f/I_b empirical criterion is inappropriate by a series experiments. Thus, the subsequent CO stripping experiment was carried out to provide better measurement of CO tolerance of our np-PtRuCuOsIr catalyst.

The CO stripping analysis provides with valuable information about the nature of electrocatalysts. Fig. 6 shows the CO stripping curves of the np-PtRuCuOsIr alloy and the commercial PtC catalyst. As shown in Fig. 6, in the first positive scan, the hydrogen oxidation charge integral is limited by the presence of adsorbed CO on the electrode surface. As the potential is swept sufficiently positive,

however, the adsorbed CO is oxidized. On the second positive scan, a hydrogen oxidation charge integral is obtained on the electrode surface free of adsorbed CO. Voltammogram for PtC shows the peak of CO oxidation at 0.67 V vs. SCE. In the case of np-PtRuCuOsIr catalyst, a broad peak appears at 0.54 V vs. SCE (Fig. 6). The lower potential (about 130 mV negative) for CO electrooxidation indicates the enhanced CO-tolerance of Pt by alloying with Ru, Cu, Os and Ir in the present np-PtRuCuOsIr catalyst. Furthermore, the obvious negative shift in peak potential is consistent with nanostructured Pt alloys [54,55].

In multi-component catalyst, Pt accomplishes the dissociative chemisorption of methanol and the alloyed 3d metals form a surface oxyhydroxide which extracts an active oxygen from the water of the acidic electrolyte. The active oxygen then oxidizes the carbonaceous residues to CO_2 [56,57]. Furthermore, the three-dimensional bi-continuous open porosity with interconnected channels and nano-sized ligaments in np-PtRuCuOsIr can provide excellent transport paths for both molecules and electrons, which can greatly facilitate the reaction kinetics. On the basis of these effects, the present np-PtRuCuOsIr alloy shows superior catalytic performance towards methanol relative to the commercial PtC catalyst.

3.3. Catalytic activity of np-PtRuCuOsIr towards ORR

In previous reports, nanoporous metallic materials prepared by the dealloying method exhibit enhanced activities towards ORR [44,58,59]. The np-PtRuCuOsIr catalyst has been proved to be with desired components and structure in nanoscale. Consequently, it is interesting to explore the ORR performance of the np-PtRuCuOsIr alloy. Fig. 7a presents the CV of the np-PtRuCuOsIr electrocatalyst in the N_2 -saturated 0.1 M HClO_4 solution. For comparison, the CV is superposed with the signal from the commercial PtC catalyst. The PtC and np-PtRuCuOsIr catalysts both display typical features which should be shown in perchloric media. In contrast, the peak position for the reduction of Pt oxides in the back scan shows a positive shift for the np-PtRuCuOsIr catalyst, indicating earlier onset of Pt–O(H) reduction [60,61]. These results also agree with our experiments at anode. Fig. 7b shows a characteristic set of polarization curves for the ORR

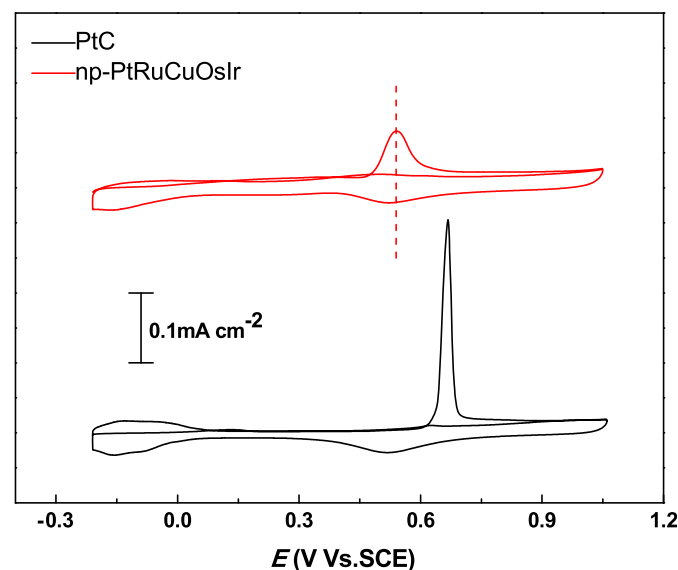


Fig. 6. Electrochemical CO-stripping curves of the np-PtRuCuOsIr and PtC catalysts in the 0.5 M H_2SO_4 solution (scan rate: 20 mV s^{-1}).

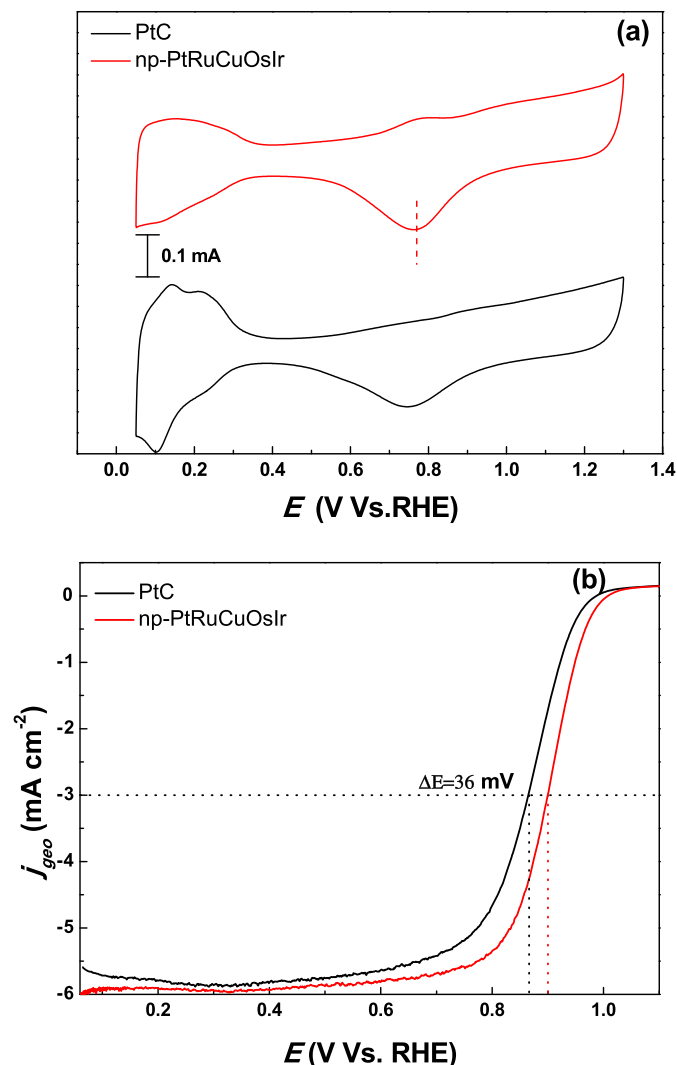


Fig. 7. (a) CV curves of the np-PtRuCuOsIr and PtC catalysts in the N_2 -purged 0.1 M $HClO_4$ solution (scan rate: $50\ mV\ s^{-1}$) and (b) ORR polarization curves for the np-PtRuCuOsIr and PtC catalysts in the O_2 -saturated 0.1 M $HClO_4$ solution at 30 °C and 1600 rpm (scan rate: $10\ mV\ s^{-1}$).

measured at 1600 rpm and normalized by the geometric area on the np-PtRuCuOsIr and PtC electrodes. It is obvious that the polarization curve of the np-PtRuCuOsIr catalyst shifts to a more positive position in comparison with PtC. At cathode, the diffusion-limited currents obtained in the potential region below 0.8 V vs. RHE suggest a four-electron transfer reaction, indicating low hydrogen peroxide formation. The mixed kinetic-diffusion control region occurs between 0.8 and 1.0 V vs. RHE [62]. The half-wave potential of the np-PtRuCuOsIr alloy is 0.900 V vs. RHE, 36 mV positive compared with that of the commercial PtC catalyst (0.864 V vs. RHE). The present results indicate a greatly enhanced ORR activity of np-PtRuCuOsIr.

Fig. 8a shows the diffusion-current-corrected Tafel plots of specific ORR activity (0.85–0.95 V vs. RHE) of the np-PtRuCuOsIr and PtC catalysts. According to the Tafel plots, the np-PtRuCuOsIr catalyst shows better specific activity than the commercial PtC at the selected potential region [58,63]. Additionally, the Tafel curve of the np-PtRuCuOsIr catalyst is parallel to that of the commercial PtC, which can be observed directly from the plots. This potential region corresponds to ORR when the adsorbed hydroxyl species (OH_{ads}) at the Pt surface determine the electrode activity. Therefore, the plots

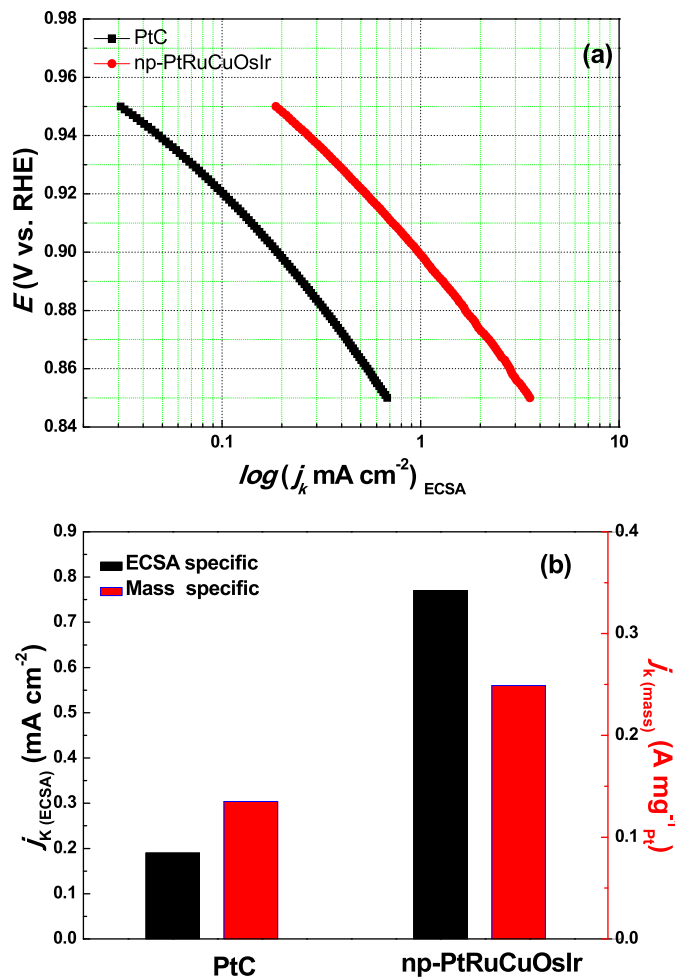


Fig. 8. (a) ECSA-normalized specific kinetic current densities (j_k) for the np-PtRuCuOsIr and PtC catalysts and (b) the ECSA- and mass-normalized specific kinetic current densities for the np-PtRuCuOsIr and PtC catalysts at 0.90 V (vs. RHE).

demonstrate the similar ORR processes on the np-PtRuCuOsIr and commercial PtC catalysts in acidic media [64,65]. The kinetic current densities at 0.90 V vs. RHE represent the intrinsic activities of electrocatalysts and were calculated by the Koutecky–Levich equation from the ORR polarization curves. The kinetic current densities were normalized by the loading amount of Pt and ECSA to obtain the mass activity and specific activity, respectively. As shown in Fig. 8b, the np-PtRuCuOsIr exhibits an outstanding specific activity of $0.77\ mA\ cm^{-2}$ and mass activity of $0.249\ A\ mg_{Pt}^{-1}$, which are ~3.8 and 1.8 times those of the commercial PtC catalyst ($0.2\ mA\ cm^{-2}$ and $0.135\ A\ mg_{Pt}^{-1}$). It should be noted that these data of the commercial PtC catalyst at the same potential are in good agreement with the reports elsewhere [16,33,44].

The ORR consists of four proton transfer and four electron transfer to each O_2 molecule ($O_2 + 4H^+ + 4e^- \rightarrow 2H_2O$) and O–O is cleaved to form OH_{ads} intermediates in this mechanism [62,66]. Alloying Pt with the 3d metals leads to smaller lattice parameter than pure Pt, which would bring about ligand and strain effects to weaken the O–O bond. This will bring about the fast scission of the O–O bond and a new bond formation between the oxygen atom and the H ion, thus increasing the O_2 reaction rate and enhancing the ORR activity [67,68]. Many groups have also argued that the d-band center of Pt-alloy shifts downwards, resulting in an increased occupancy of the O 2p and Pt 5d anti-bonding states which would bind OH_{ads} species more weakly [69,70]. These results are also

consistent with the d-band model [71] and can explain the observed ORR activity enhancement of the np-PtRuCuOsIr alloy.

Fig. 9 shows the CV curves, ORR polarization curves and corresponding specific activities of the np-PtRuCuOsIr alloy after different cycles (10, 10 K and 15 K). The CV measurements show a loss of 19.1% and 36.9% in the ECSA for the np-PtRuCuOsIr after 10 K and 15 K cycles, respectively (Fig. 9a). The np-PtRuCuOsIr had no substantial change in diffusion-limited current in the polarization curve and a negative shift in the half-wave potential of 15 mV and

25 mV, after 10 K and 15 K cycles respectively, compared to the initial polarization curve (Fig. 9b). As illustrated in Fig. 9c, the ECSA specific activity maintains 90.3% and 73.1% of the initial value after 10 K and 15 K cycles, respectively. Accordingly, the mass activity decreases to 70.2% and 50.0%. The np-PtRuCuOsIr shows better durability in comparison with the commercial PtC catalyst under similar testing conditions [33,44]. The possible dissolution, aggregation and Ostwald ripening processes would lead to the loss of ECSA and catalytic activity of electrocatalysts [26]. The coarsening of the nanoporous structure is related to the surface diffusion of metal elements, which follows the power law decay proportional to a quarter order of time [72]. However, the coarsening of this three-dimensional bi-continuous interpenetrating ligament/channel structure can be dramatically deferred with the ligaments evolving to a larger size [72]. Furthermore, the important degradation mechanisms of alloy nanoparticles are dependent on their initial compositions. The Pt-skin covering the ligament surface in the np-PtRuCuOsIr could suppress its structure coarsening due to the strain effect [58,67].

As for the present fabrication strategy, the following issues should also be taken into consideration. Although our np-PtRuCuOsIr catalyst exhibits enhanced electrocatalytic activities towards MOR and ORR, the final catalyst failed to be thoroughly alloyed with ruthenium as expected. And there is also some nonuniform component in the np-PtRuCuOsIr catalyst. In addition, the as-obtained catalysts are powder-like, and the size of these powders ranges from dozens of nanometers to several microns, which are a little big for MOR and ORR reactions.

4. Conclusions

In summary, we have successfully fabricated a nanoporous PtRuCuOsIr catalyst by mild chemical dealloying of the mechanically alloyed precursor powders. The np-PtRuCuOsIr catalyst with a three-dimensional bi-continuous ligament/channel structure shows enhanced catalytic activity for methanol electro-oxidation as well as CO tolerance at anode, compared to the commercial PtC catalyst. Moreover, the catalyst also shows greatly enhanced catalytic activity and durability towards oxygen reduction reaction at cathode. Our results provide a novel strategy for design of precursor alloys and fabrication of multi-component nanoporous alloy catalysts for DMFCs.

Acknowledgments

The authors gratefully acknowledge financial support by National Natural Science Foundation of China (51371106), National Basic Research Program of China (973, 2012CB932800), Open Project of Shanghai Key Laboratory of Modern Metallurgy and Materials Processing (SELF-2011-02), Program for New Century Excellent Talents in University (MOE, NCET-11-0318), Specialized Research Fund for the Doctoral Program of Higher Education of China (20120131110017), and Young Top-top Talent Support Project (the Organization Department of the Central Committee of the CPC). Z.H Zhang also acknowledges the support from the Alexander von Humboldt Foundation, Germany.

References

- [1] B.D. McNicol, D.A.J. Rand, K.R. Williams, *J. Power Sources* 83 (1999) 15–31.
- [2] R. Liu, E.S. Smotkin, *J. Electroanal. Chem.* 535 (2002) 49–55.
- [3] Z.-B. Wang, C.-R. Zhao, P.-F. Shi, Y.-S. Yang, Z.-B. Yu, W.-K. Wang, G.-P. Yin, *J. Phys. Chem. C* 114 (2009) 672–677.
- [4] J.N. Tiwari, R.N. Tiwari, G. Singh, K.S. Kim, *Nano Energy* 2 (2013) 553–578.
- [5] S.K. Kamarudin, F. Achmad, W.R.W. Daud, *Int. J. Hydrogen Energy* 34 (2009) 6902–6916.

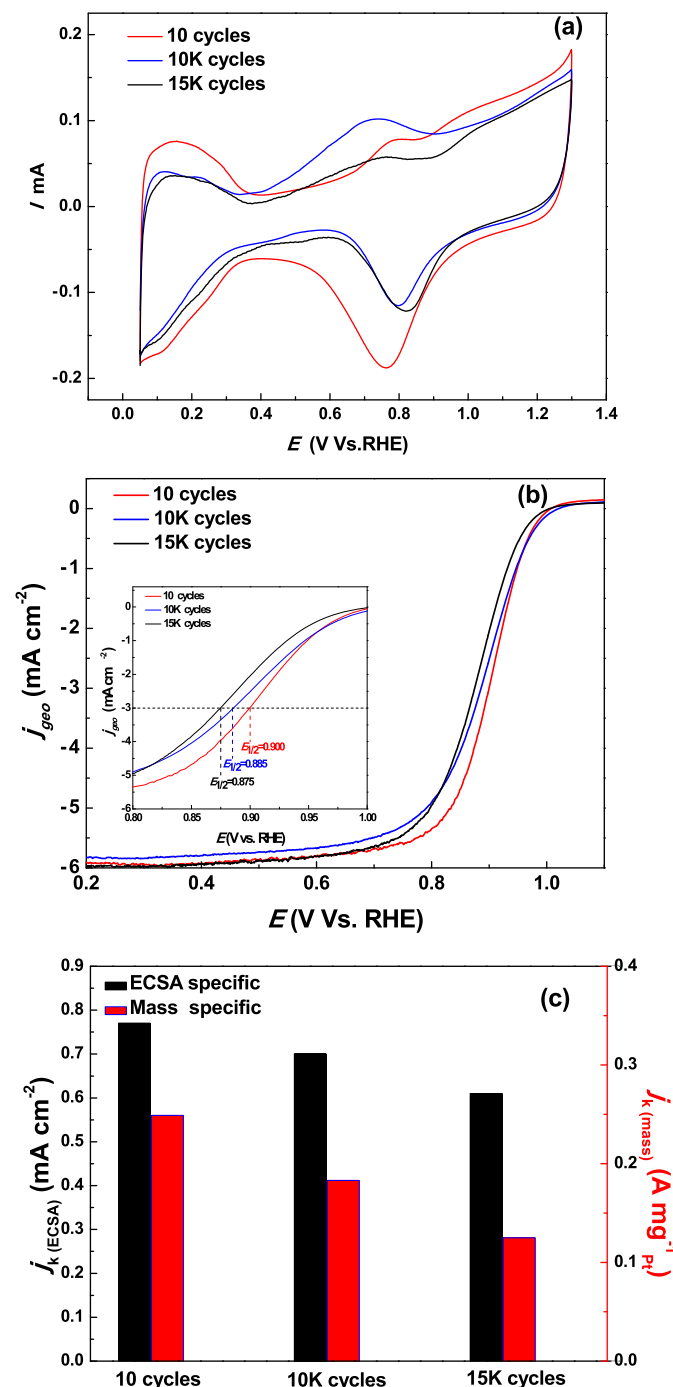


Fig. 9. (a) CVs and (b) ORR polarization curves for the np-PtRuCuOsIr catalyst after 10, 10 K and 15 K potential cycles in the 0.1 M HClO₄ solution. Inset in (b): half-wave potentials highlighted by dotted lines. (c) The ECSA- and mass-normalized specific kinetic current densities for the np-PtRuCuOsIr at 0.90 V (vs. RHE).

- [6] E. Reddington, A. Sapienza, B. Gurau, R. Viswanathan, S. Sarangapani, E.S. Smotkin, T.E. Mallouk, *Science* 280 (1998) 1735–1737.
- [7] Y.H. Lee, G. Lee, J.H. Shim, S. Hwang, J. Kwak, K. Lee, H. Song, J.T. Park, *Chem. Mater.* 18 (2006) 4209–4211.
- [8] S.H. Ahn, I. Choi, O.J. Kwon, J.J. Kim, *Biochem. Eng. J.* 181–182 (2012) 276–280.
- [9] Z. Liu, J.Y. Lee, M. Han, W. Chen, L.M. Gan, *J. Mater. Chem.* 12 (2002) 2453–2458.
- [10] S.-I. Choi, S. Xie, M. Shao, J.H. Odell, N. Lu, H.-C. Peng, L. Protsailo, S. Guerrero, J. Park, X. Xia, J. Wang, M.J. Kim, Y. Xia, *Nano Lett.* 13 (2013) 3420–3425.
- [11] C. Wang, N.M. Markovic, V.R. Stamenkovic, *ACS Catal.* 2 (2012) 891–898.
- [12] R. Ahmadi, M.K. Amini, J.C. Bennett, *J. Catal.* 292 (2012) 81–89.
- [13] X. Ma, L. Luo, L. Zhu, L. Yu, L. Sheng, K. An, Y. Ando, X. Zhao, *J. Power Sources* 241 (2013) 274–280.
- [14] S. Koh, P. Strasser, *J. Am. Chem. Soc.* 129 (2007) 12624–12625.
- [15] Y.-W. Lee, A.R. Ko, S.-B. Han, H.-S. Kim, K.-W. Park, *Phys. Chem. Chem. Phys.* 13 (2011) 5569–5572.
- [16] Y.-H. Cho, O.-H. Kim, D.Y. Chung, H. Choe, Y.-H. Cho, Y.-E. Sung, *Appl. Catal. B* 154–155 (2014) 309–315.
- [17] L. Zou, J. Guo, J. Liu, Z. Zou, D.L. Akins, H. Yang, *J. Power Sources* 248 (2014) 356–362.
- [18] J.W. Guo, T.S. Zhao, J. Prabhuram, R. Chen, C.W. Wong, *Electrochim. Acta* 51 (2005) 754–763.
- [19] Z. Jusys, T.J. Schmidt, L. Dubau, K. Lasch, L. Jörissen, J. Garche, R.J. Behm, *J. Power Sources* 105 (2002) 297–304.
- [20] C.Z. He, H.R. Kunz, J.M. Fenton, *J. Electrochem. Soc.* 144 (1997) 970–979.
- [21] H. Liu, C. Song, L. Zhang, J. Zhang, H. Wang, D.P. Wilkinson, *J. Power Sources* 155 (2006) 95–110.
- [22] J.F. Whitacre, T. Valdez, S.R. Narayanan, *J. Electrochem. Soc.* 152 (2005) A1780–A1789.
- [23] T.S. Almeida, L.M. Palma, P.H. Leonello, C. Morais, K.B. Kokoh, A.R. De Andrade, *J. Power Sources* 215 (2012) 53–62.
- [24] Z. Liu, L. Hong, S.W. Tay, *Mater. Chem. Phys.* 105 (2007) 222–228.
- [25] Z. Liu, X.Y. Ling, X. Su, J.Y. Lee, *J. Phys. Chem. B* 108 (2004) 8234–8240.
- [26] L. Liu, Z. Huang, D. Wang, R. Scholz, E. Pippel, *Nanotechnol* 22 (2011) 105604.
- [27] M. Ammam, E.B. Easton, *J. Power Sources* 215 (2012) 188–198.
- [28] Z. Zhang, Y. Wang, X. Wang, *Nanoscale* 3 (2011) 1663–1674.
- [29] J. Erlebacher, M.J. Aziz, A. Karma, N. Dimitrov, K. Sieradzki, *Nature* 410 (2001) 450–453.
- [30] T. You, O. Niwa, M. Tomita, S. Hirono, *Anal. Chem.* 75 (2003) 2080–2085.
- [31] J. Weissmüller, R.N. Viswanath, D. Kramer, P. Zimmer, R. Würschum, H. Gleiter, *Science* 300 (2003) 312–315.
- [32] Z. Qi, H. Geng, X. Wang, C. Zhao, H. Ji, C. Zhang, J. Xu, Z. Zhang, *J. Power Sources* 196 (2011) 5823–5828.
- [33] C. Xu, Y. Liu, Q. Hao, H. Duan, *J. Mater. Chem. A* 1 (2013) 13542–13548.
- [34] Y. Wang, Y. Wang, C. Zhang, T. Kou, Z. Zhang, *CrystEngComm* 14 (2012) 8352–8356.
- [35] X. Wang, W. Wang, Z. Qi, C. Zhao, H. Ji, Z. Zhang, *Int. J. Hydrogen Energy* 37 (2012) 2579–2587.
- [36] M. Hakamada, M. Mabuchi, *J. Alloys Compd.* 479 (2009) 326–329.
- [37] H. Qiu, Z. Zhang, X. Huang, Y. Qu, *ChemPhysChem* 12 (2011) 2118–2123.
- [38] C. Zhang, J. Sun, J. Xu, X. Wang, H. Ji, C. Zhao, Z. Zhang, *Electrochim. Acta* 63 (2012) 302–311.
- [39] C. Xu, L. Wang, R. Wang, K. Wang, Y. Zhang, F. Tian, Y. Ding, *Adv. Mater.* 21 (2009) 2165–2169.
- [40] J. Zhang, H. Ma, D. Zhang, P. Liu, F. Tian, Y. Ding, *Phys. Chem. Chem. Phys.* 10 (2008) 3250–3255.
- [41] Z. Zhang, C. Zhang, J. Sun, T. Kou, Q. Bai, Y. Wang, Y. Ding, *J. Mater. Chem. A* 1 (2013) 3620–3628.
- [42] X. Chen, Y. Jiang, J. Sun, C. Jin, Z. Zhang, *J. Power Sources* 267 (2014) 212–218.
- [43] A. Brouzgou, S.Q. Song, P. Tsiakaras, *Appl. Catal. B* 127 (2012) 371–388.
- [44] R. Wang, C. Xu, X. Bi, Y. Ding, *Energy Environ. Sci.* 5 (2012) 5281–5286.
- [45] H. Zhu, S. Zhang, S. Guo, D. Su, S. Sun, *J. Am. Chem. Soc.* 135 (2013) 7130–7133.
- [46] H.-H. Li, C.-H. Cui, S. Zhao, H.-B. Yao, M.-R. Gao, F.-J. Fan, S.-H. Yu, *Adv. Energy Mater.* 2 (2012) 1182–1187.
- [47] A. Takeuchi, A. Inoue, *Mater. Trans.* 46 (2005) 2817–2829.
- [48] A. Pozio, M. De Francesco, A. Cembali, F. Cardellini, L. Giorgi, *J. Power Sources* 105 (2002) 13–19.
- [49] C.-H. Cui, S.-H. Yu, *Acc. Chem. Res.* 46 (2013) 1427–1437.
- [50] S.J. Yoo, T.-Y. Jeon, K.S. Kim, T.-H. Lim, Y.-E. Sung, *Phys. Chem. Chem. Phys.* 12 (2010) 15240–15246.
- [51] Y. Wang, C. He, A. Brouzgou, Y. Liang, R. Fu, D. Wu, P. Tsiakaras, S. Song, *J. Power Sources* 200 (2012) 8–13.
- [52] R. Mancharan, J.B. Goodenough, *J. Mater. Chem.* 2 (1992) 875–887.
- [53] A.M. Hofstead-Duffy, D.-J. Chen, S.-G. Sun, Y.J. Tong, *J. Mater. Chem.* 22 (2012) 5205–5208.
- [54] K. Wang, Y. Wang, Z. Liang, Y. Liang, D. Wu, S. Song, P. Tsiakaras, *Appl. Catal. B* 147 (2014) 518–525.
- [55] T. Arikian, A.M. Kannan, F. Kadirgan, *Int. J. Hydrogen Energy* 38 (2013) 2900–2907.
- [56] K.L. Ley, R. Liu, C. Pu, Q. Fan, N. Leyarovska, C. Segre, E.S. Smotkin, *J. Electrochem. Soc.* 144 (1997) 1543–1548.
- [57] H.-W. Lei, S. Suh, B. Gurau, B. Workie, R. Liu, E.S. Smotkin, *Electrochim. Acta* 47 (2002) 2913–2919.
- [58] R. Yang, J. Leisch, P. Strasser, M.F. Toney, *Chem. Mater.* 22 (2010) 4712–4720.
- [59] D. Wang, Y. Yu, H.L. Xin, R. Hovden, P. Ercius, J.A. Mundy, H. Chen, J.H. Richard, D.A. Muller, F.J. DiSalvo, H.D. Abruna, *Nano Lett.* 12 (2012) 5230–5238.
- [60] M. Khosravi, M.K. Amini, *Int. J. Hydrogen Energy* 35 (2010) 10527–10538.
- [61] I. Dutta, M.K. Carpenter, M.P. Balogh, J.M. Ziegelbauer, T.E. Moylan, M.H. Atwan, N.P. Irish, *J. Phys. Chem. C* 114 (2010) 16309–16320.
- [62] I.E.L. Stephens, A.S. Bondarenko, U. Gronbjerg, J. Rossmeisl, I. Chorkendorff, *Energy Environ. Sci.* 5 (2012) 6744–6762.
- [63] R. Yang, W. Bian, P. Strasser, M.F. Toney, *J. Power Sources* 222 (2013) 169–176.
- [64] Y. Hu, J.O. Jensen, W. Zhang, L.N. Cleemann, W. Xing, N.J. Bjerrum, Q. Li, *Angew. Chem. Int. Ed.* 53 (2014) 3675–3679.
- [65] A. Kongkanand, S. Kuwabata, G. Girishkumar, P. Kamat, *Langmuir* 22 (2006) 2392–2396.
- [66] S. Guo, S. Zhang, S. Sun, *Angew. Chem. Int. Ed.* 52 (2013) 8526–8544.
- [67] T. Toda, H. Igarashi, H. Uchida, M. Watanabe, *J. Electrochem. Soc.* 146 (1999) 3750–3756.
- [68] T. Toda, H. Igarashi, M. Watanabe, *J. Electrochem. Soc.* 145 (1998) 4185–4188.
- [69] I.E.L. Stephens, A.S. Bondarenko, F.J. Perez-Alonso, F. Calle-Vallejo, L. Bech, T.P. Johansson, A.K. Jepsen, R. Frydendal, B.P. Knudsen, J. Rossmeisl, I. Chorkendorff, *J. Am. Chem. Soc.* 133 (2011) 5485–5491.
- [70] P. Strasser, S. Koh, T. Anniyev, J. Greeley, K. More, C. Yu, Z. Liu, S. Kaya, D. Nordlund, H. Ogasawara, M.F. Toney, A. Nilsson, *Nat. Chem.* 2 (2010) 454–460.
- [71] M. Mavrikakis, B. Hammer, J.K. Nørskov, *Phys. Rev. Lett.* 81 (1998) 2819–2822.
- [72] J. Erlebacher, *J. Electrochem. Soc.* 151 (2004) C614–C626.